photonics

MDPI

Article

Experimental Analysis of Channel Interleaving in Photon-Counting Communication over a 12-km Terrestrial Free-Space Optical Link

Xintong Guo [1,2,3], Han Bao [3], Chengxiang Tu [1,2,3], Zhenyu Li [1,2], Jincai Wu [1,3,4], Xingyue Wang [1,2], Xin Yu [1,2,3], Yunpeng Liu [1], Yuefeng Li [4], Jun Huang [1,4,*], Liang Zhang [1,3,4] and Jianyu Wang [1,3,4,*]

[1] Key Laboratory of Space Active Opto-Electronics Technology, Shanghai Institute of Technical Physics, Chinese Academy of Sciences, Shanghai 200083, China; guoxintong20@mails.ucas.ac.cn (X.G.); tuchengxiang25@mails.ucas.ac.cn (C.T.); lizhenyu241@mails.ucas.ac.cn (Z.L.); jcwu@mail.sitp.ac.cn (J.W.); wangxingyue22@mails.ucas.ac.cn (X.W.); yuxin24@mails.ucas.ac.cn (X.Y.); liuyunpeng@mail.sitp.ac.cn (Y.L.); zhliang@mail.sitp.ac.cn (L.Z.)
[2] University of Chinese Academy of Sciences, Beijing 100049, China
[3] Hefei National Laboratory, Hefei 230088, China; baohansc@mail.ustc.edu.cn
[4] Shanghai Research Center for Quantum Science, Shanghai 201315, China; liyuefeng@hfnl.cn
* Correspondence: huangjun@mail.sitp.ac.cn (J.H.); jywang@mail.sitp.ac.cn (J.W.)

Abstract

In lunar and deep-space optical communication uplinks, atmospheric turbulence can induce temporally correlated fades in photon-limited free-space optical (FSO) channels. These fades can lead to burst errors and consequently degrade the reliability of coded transmission. In this work, we conducted a 12 km urban horizontal free-space PPM communication experiment using a room-temperature single-photon detector. The acquired photon-counting data were used to characterize the scintillation and fade-duration statistics of the atmospheric channel. We further compared the communication performance of different channel interleaving schemes under the same link conditions. At a data rate of 25.8 Mbps, the Matrix-128 scheme achieved a receiver sensitivity of 0.86 detected photons per bit at the lowest operating point with zero observed bit errors, corresponding to a 2.64 dB sensitivity improvement over the non-interleaved scheme. The experimental results show that channel interleaving effectively disperses turbulence-induced burst errors and improves the receiver sensitivity of the high-speed photon-counting PPM system. This experiment provides field experimental evidence for evaluating the performance of channel interleaving and selecting interleaving parameters for uplink photon-counting communication under realistic atmospheric turbulence conditions.

Keywords: free-space optical communication; photon-counting communication; atmospheric turbulence; channel interleaving

Check for updates

Received: 4 September 2026
Revised: 24 September 2026
Accepted: 28 September 2026
Published: 30 September 2026

Copyright: © 2026 by the authors. Licensee MDPI, Basel, Switzerland. This article is an open access article distributed under the terms and conditions of the Creative Commons Attribution (CC BY) license.

1. Introduction

Long-haul free-space optical (FSO) communication links suffer from beam divergence, pointing loss, and atmospheric attenuation, among other propagation impairments, which can drive the receiver into a photon-limited operating regime [1]. Photon-counting receivers employ single-photon detectors to record photon arrival events from weak optical signals, enabling high receiver sensitivity at extremely low received power levels [2,3]. Pulse-position modulation (PPM) concentrates the optical pulse energy into a single time slot within each symbol period and offers relatively high photon efficiency, making it well

suited for photon-limited long-haul optical communication [4,5]. In recent years, space laser communication missions such as LLCD, DSOC, and O2O have demonstrated optical communication capabilities over lunar and deep-space links [6–8].

For lunar and deep-space optical downlinks, photon-counting receivers equipped with superconducting nanowire single-photon detectors (SNSPDs) have realized data rates on the order of gigabits per second (Gbps) [9] and have been deployed in the DSOC ground reception system [10]. However, SNSPDs require operation at cryogenic temperatures, and the accompanying cooling and support subsystems add considerable engineering complexity to the receiver [10]. For optical uplink scenarios, the LLCD mission adopted 4-PPM and achieved a lunar uplink data rate of approximately 20 Mbps [6], with an optically preamplified direct-detection receiver aboard the spacecraft [11]. The 32-PPM uplink of O2O supports two data rate mode of 10 and 20 Mbps [12]. Although the DSOC mission adopts Geiger-mode photon-counting detection technology aboard the spacecraft, its uplink data rate is only approximately 1.6 kbps [7]. Therefore, space optical uplinks with data rates on the order of tens of Mbps remain predominantly reliant on non-photon-counting direct-detection receivers. In contrast to cryogenically cooled SNSPDs, room-temperature single-photon detectors remove the requirement for cryogenic cooling, making them far more appealing for spacecraft with strict size, weight, and power (SWaP) constraints. Prior SPAD-based photon-counting communication demonstrations have achieved data rates up to 50 Mbps, with a corresponding receiver sensitivity of approximately 4 photons per bit [13]. In contrast, a single-pixel SPAD paired with SCPPM delivers a single-photon-level sensitivity of 1.35 photons per bit, albeit at a lower data rate of approximately 6.21 Mbps [14]. Therefore, high-speed optical uplinks based on room-temperature single-photon detection are poised to emerge as a key development direction for future photon-limited uplink communication systems.

For ground-to-space optical uplinks, atmospheric turbulence-induced scintillation and beam wander, together with system pointing errors, can cause temporal fluctuations in the received optical intensity and photon count rate [1,15,16]. Because atmospheric turbulence exhibits temporal correlation, persistent deep fades may span multiple high-rate PPM symbols, resulting in temporally correlated errors and burst error events. Such burst errors can reduce the effectiveness of FEC coding and may not be fully mitigated by coding alone [17]. Channel interleaving reorders encoded symbols in the time domain, spreading adjacent symbols from the same codeword across distinct transmission instants. Following deinterleaving, consecutive fading-induced errors are dispersed across different data positions, thereby reducing the clustering of burst errors within a single SCPPM codeword and enhancing the communication system's resilience to turbulence-induced fading [18].

Prior studies on channel interleaving for FSO links have verified the efficacy of this technique in mitigating turbulence-induced fading across various communication schemes. For conventional intensity-modulation/direct-detection (IM/DD) systems, Greco demonstrated error-free transmission over a 5.4 km terrestrial FSO link under strong scintillation using FEC and interleaving [19]. Fujita et al. showed that block interleaving improved the error-correction performance over a 7.8 km terrestrial FSO link [20]. Chang et al. further demonstrated reductions in BER and outage probability using deep interleaving over a 7 km FSO link [21]. Sun and Noh further demonstrated that system performance depends on the degree of matching between the interleaving depth and the channel coherence time [17]. In coherent FSO systems, Boddeda et al. examined the impacts of data interleaving on both system throughput and latency in the presence of atmospheric turbulence [22]. Gümüş et al. analyzed the required interleaving lengths under different turbulence conditions using long-term measurement data from a 4.6 km FSO experimental link [23]. For photon-

counting communication, Burton et al. investigated channel-interleaving performance for deep-space SCPPM links via simulations [24], while Downey et al. further demonstrated the effectiveness of convolutional interleaving using real-time photon-counting reception under emulated fading conditions [25]. Overall, channel interleaving has been experimentally demonstrated over real atmospheric links in conventional FSO and coherent optical communication systems. In contrast, studies on photon-counting communication have mainly relied on numerical simulations and experiments with emulated atmospheric fading. Therefore, the effectiveness of channel interleaving in long-haul atmospheric photon-counting links using room-temperature single-photon detectors still requires further experimental validation.

In this work, we investigate the effectiveness of channel interleaving for turbulence mitigation in high-speed photon-limited optical uplinks. A 12 km urban horizontal free-space PPM communication link was established using a room-temperature single-photon detector, achieving a data rate of 25.8 Mbps. The received photon-counting data were used to characterize the scintillation and fade-duration statistics of the atmospheric channel. Under the same link conditions, we compared the communication performance of the non-interleaved scheme, matrix interleavers with different depths, and convolutional interleavers with different parameter settings. We further evaluated how the interleaver structure and interleaving scale affect system performance under atmospheric turbulence. The results provide experimental support for performance evaluation and interleaver parameter design in high-speed photon-limited PPM links using room-temperature single-photon detection.

2. Materials and Methods

2.1. Experimental Setup and Data Acquisition

A 12 km terrestrial free-space optical (FSO) communication link was established between two buildings. Figure 1 shows the link locations and the optical system architectures at the transmitter and receiver. As shown in Figure 1a, the transmitter and receiver were separated by approximately 12 km along an urban horizontal propagation path. Figures 1b and 1c show the optical layouts of the transmitter and receiver, respectively. Although this horizontal link differs from an actual satellite-to-ground uplink in terms of propagation geometry and the spatial distribution of atmospheric turbulence, long-haul near-ground propagation can experience pronounced turbulence effects. Therefore, the link provides a terrestrial field-test platform for evaluating the performance of photon-limited optical communication systems under atmospheric turbulence.

The main parameters of the experimental link are summarized in Table 1. Room-temperature near-infrared single-photon detectors can be limited in high-speed photon-counting applications by dead time and afterpulsing [26]. In contrast, visible-band silicon single-photon avalanche diodes (Si-SPADs) can provide high detection efficiency and high count-rate capability at room temperature [27]. Therefore, we selected a wavelength of 450 nm for the communication signal to enable high-speed photon-counting reception. The communication experiment employed 16-PPM with rate-1/2 SCPPM coding. The slot rate was set to 400 MHz, and 15 guard slots were appended to each 16-PPM symbol. Accordingly, each slot had a duration of 2.5 ns, resulting in a 37.5 ns guard interval. This interval is longer than the nominal dead time of 24 ns for the single-photon detector. Even when the valid pulses in two adjacent PPM symbols have the minimum temporal separation, the guard slots provide sufficient time for the detector to recover after a valid detection event. This reduces the loss of subsequent photon counts caused by detector dead time. With this configuration, each PPM symbol occupies 77.5 ns. Combined with the rate-1/2 SCPPM code, the resulting information data rate is 25.8 Mbps. Therefore, the adopted modulation, coding,

and symbol structure enable high-speed photon-counting transmission while accounting for the constraint imposed by detector dead time on successive photon detections.

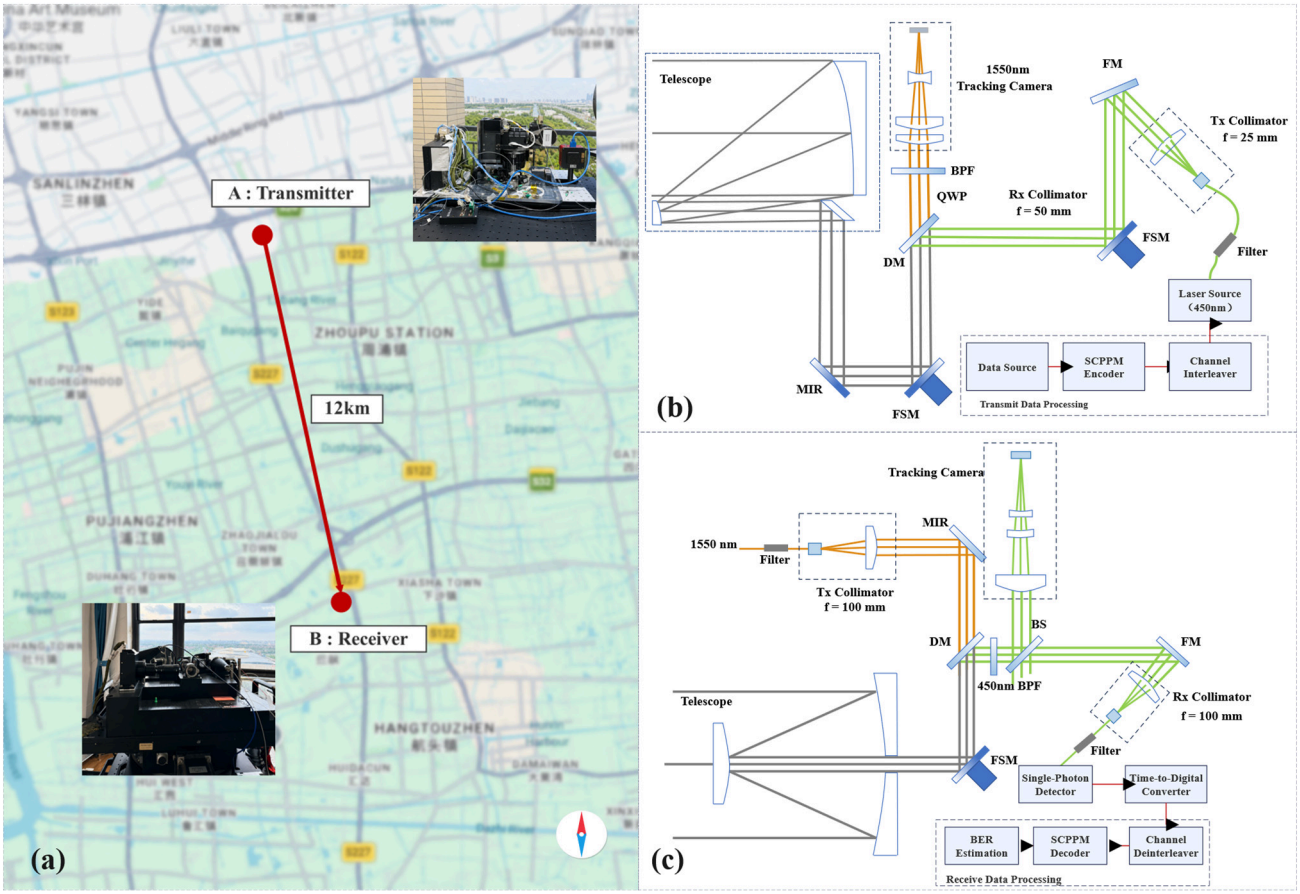


Figure 1. (**a**) 12 km experimental FSO link (map data © 2026 Google). (**b**) schematic of the transmitter. (**c**) schematic of the receiver. (BPF: band-pass filter; QWP: quarter-wave plate; DM: dichroic mirror; MIR: mirror; FSM: fast steering mirror; FM: fold mirror; BS: beam splitter).

Table 1. Main parameters of the experimental link.

Category	Parameter	Value
Transmitter	Signal wavelength	450 nm
	Transmitter aperture diameter	60 mm
	Signal beam divergence angle	47.36 μrad
Receiver	Beacon wavelength	1550 nm
	Receiver aperture diameter	100 mm
	Receiver fiber core diameter	62.5 μm
	Beacon beam divergence angle	76.20 μrad
Communication system	Link distance	12 km
	PPM order	16
	Number of guard slots	15
	Slot rate	400 MHz
	Data rate	25.8 Mbps

The original data were sequentially processed by SCPPM encoding and channel interleaving to generate the data sequence for transmission, followed by PPM. The modulated 450 nm signal beam was collimated by the transmit optics and launched into the free-space channel. To maintain stable pointing of the signal beam, the transmitter was also equipped

with a 1550 nm beacon-receiving and tracking path. The 1550 nm beacon beam transmitted from the receiver was collected by the telescope, separated from the communication optical path by a dichroic mirror, and imaged onto the tracking camera. Based on the measured position of the beacon spot, the fine-pointing mechanism performed real-time correction of the optical axis, thereby maintaining stable alignment of the transmitted beam with the receiver terminal.

After propagation through the 12 km atmospheric channel, the 450 nm signal beam was collected by the receiver telescope and directed to the single-photon detector after fine pointing, filtering and coupling, enabling photon-counting reception of the weak optical signal. The receiver was also equipped with a 1550 nm beacon-transmission path to provide the beacon beam required for acquisition and tracking at the transmitter. Meanwhile, the tracking camera at the receiver captured the tracking spot transmitted from the transmitter, and the fine-pointing mechanism corrected the optical axis according to the measured spot-position error. Through coordinated operation of the transmitter and receiver, stable communication and beacon-tracking optical paths were established.

The fine-pointing mechanisms at both the transmitter and receiver use fast-steering mirrors (FSMs) based on two-axis piezoelectric tip/tilt platforms (S-330.4SH, Physik Instrumente, Karlsruhe, Germany) for beam-angle correction. The closed-loop fine-tracking control structure is shown in Figure 2. The device employs piezoelectric actuation with flexure guidance and provides a two-axis angular range of 5 mrad. The tracking camera continuously measures the centroid position of the optical spot on the detector plane, and the deviation of the centroid from the reference position is used to generate the pointing-error signal. After processing by the controller, this error signal drives the FSM to adjust the mirror angle, thereby providing closed-loop correction of the beam propagation direction. A proportional–integral controller was used in the fine-tracking loop, with a closed-loop command update rate of 2 kHz. The compensation capability of the fine-tracking loop for spot-position variations is jointly determined by the dynamic response of the FSM, the sampling process of the tracking camera, and the control update rate.

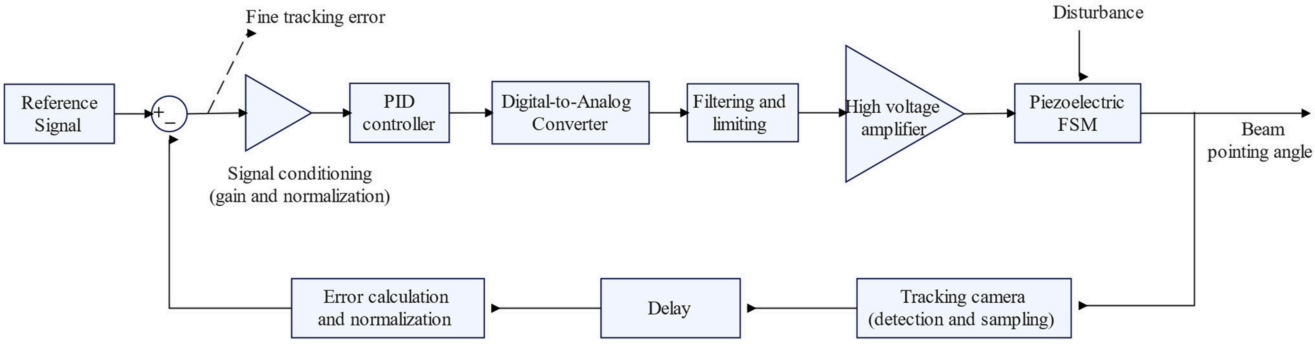


Figure 2. Fine-Tracking Control System Block Diagram.

To evaluate the influence of tracking-beam power on closed-loop tracking performance, a link power analysis was performed for the tracking optical paths at both the transmitter and receiver. The received optical power at the tracking-camera detector plane can be expressed as [28]

$$P_{cam} = P_t \eta_t \eta_{geo} \eta_{tr} \eta_{atm} \eta_r \quad (1)$$

where P_t is the transmitted optical power, η_t and η_r are the overall optical efficiencies of the transmitter and receiver, respectively, η_g is the geometric transmission efficiency, η_a is the atmospheric transmission efficiency, and η_{tr} is the tracking efficiency. Considering

beam expansion during free-space propagation, the geometric transmission efficiency can be expressed as [29]

$$\eta_{\text{geo}} = \left(\frac{D_r}{D_t + L\theta} \right)^2 \tag{2}$$

where D_t and D_r are the transmit and receive aperture diameters, respectively, L is the link distance, and θ is the full-angle beam divergence.

2.2. Channel Interleaving and Photon-Counting Data Processing

Practical free-space optical (FSO) links are susceptible to atmospheric turbulence. Temporally correlated fading of the received signal can impair consecutive symbols and lead to burst errors [17]. Channel interleaving mitigates the impact of such burst errors on SCPPM decoding by rearranging consecutive symbols in the time domain. As a result, burst errors are distributed across different codewords, reducing the concentration of errors within each codeword [18]. Common channel interleaving schemes include block, random, and convolutional interleaving [30]. In this work, matrix and convolutional interleaving schemes were selected for experimental comparison. Matrix interleaving features a simple structure and straightforward implementation, whereas convolutional interleaving distributes consecutive symbols over time through multiple branches with different delays. The basic principles of the two interleaving schemes are illustrated in Figure 2.

As shown in Figure 3a, matrix interleaving rearranges the encoded symbols by changing the order in which they are written to and read from the interleaving matrix [17]. D consecutive SCPPM codewords are written row-wise into a two-dimensional interleaving matrix and read out column-wise, where D denotes the interleaving depth and S is the number of PPM symbols in each SCPPM codeword. In this way, symbols that are originally adjacent in time are redistributed to different transmission positions. As shown in Figure 3b, the convolutional interleaver consists of N parallel branches with different delays [24]. The input PPM symbols are sequentially routed to these branches and output after different delays, thereby dispersing consecutive symbols in the time domain. For the convolutional interleaver used in this work, the delay of the i-th branch is determined by the delay increment B between adjacent branches, resulting in progressively increasing temporal delays across the branches.

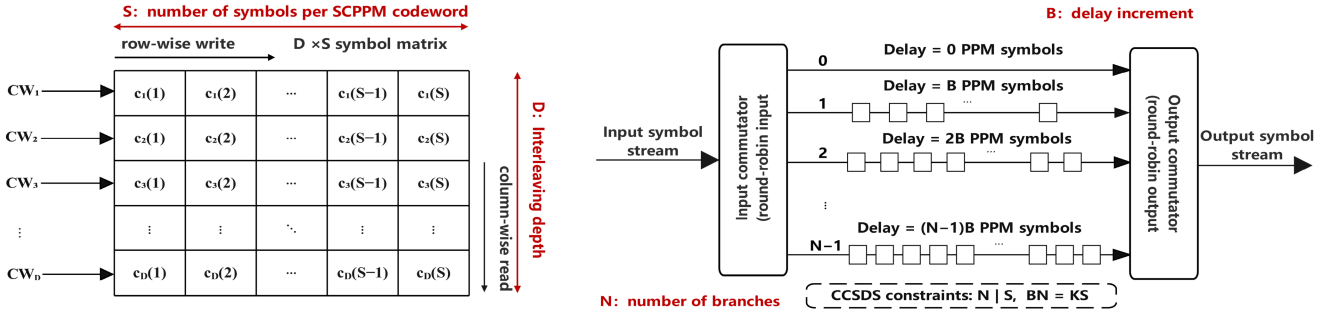


Figure 3. Schematic diagrams of (**a**) matrix interleaving and (**b**) convolutional interleaving.

For a fixed data rate and modulation format, increasing the interleaving span extends the time interval over which consecutive symbols are dispersed. This can improve the mitigation of temporally correlated fading, but at the cost of increased interleaving delay and memory requirements [17,18]. Therefore, we tested multiple matrix and convolutional interleaving configurations with different interleaving spans and compared their communication performance under the same link conditions.

To characterize the implementation overhead of different interleaving configurations, the theoretical buffer requirement was calculated according to the corresponding interleaver structure. For matrix interleaving, the interleaving matrix contains N_M PPM symbols, and the required buffer size is given by [31]

$$M_{\text{mat}} = DS \tag{3}$$

where $S = 3780$ denotes the number of PPM symbols contained in one SCPPM codeword. For convolutional interleaving, the delay of the ith branch is D_i. Therefore, the total delay-storage requirement can be expressed as [31]

$$M_{\text{conv}} = \sum_{i=0}^{N-1} iB = \frac{BN(N-1)}{2} \tag{4}$$

The theoretical buffer requirements for the different interleaving configurations are summarized in Table 2.

Table 2. Parameters and Theoretical Buffer Requirements for Different Interleaving Schemes.

Interleaving Scheme	Parameters	Theoretical Buffer Requirement (PPM Symbols)
Matrix-32	D = 32, S = 3780	120,960
Matrix-64	D = 64, S = 3780	241,920
Matrix-128	D = 128, S = 3780	483,840
Conv-15	N = 15, B = 252	26,460
Conv-30	N = 30, B = 126	54,810
Conv-63	N = 63, B = 60	117,180

The arrival times of single-photon detection events were recorded by the TDC at the receiver, and the communication data were processed offline. Frame synchronization and PPM slot decisions were performed based on the photon arrival times to obtain the received PPM symbol sequence. The sequence was then deinterleaved according to the interleaving structure used at the transmitter, followed by SCPPM decoding. The SCPPM receiver employed an iterative decoding structure based on the BCJR algorithm, and the a posteriori log-likelihood ratio (LLR) of each information bit was calculated from the received observations [4]. For the kth information bit, the a posteriori LLR can be expressed as [24]

$$L(u_k) = \ln \frac{P(u_k = 1 \mid \boldsymbol{y})}{P(u_k = 0 \mid y)} \tag{5}$$

where y denotes the received observation sequence. After several decoding iterations, a hard decision is made on each information bit according to the final LLR:

$$\hat{u}_k = \begin{cases} 1, & L(u_k) > 0 \\ 0, & L(u_k) \leq 0 \end{cases} \tag{6}$$

Finally, the decoded information-bit sequence was compared bit by bit with the original transmitted information-bit sequence, and the bit error rate (BER) after SCPPM decoding was defined as

$$\text{BER}_{\text{SCPPM}} = \frac{1}{K} \sum_{k=1}^{K} \mathbf{1}\left(\hat{u}_k \neq u_k\right) = \frac{N_{\text{err}}}{K} \tag{7}$$

where K is the total number of information bits included in the BER calculation, N_{err} is the number of erroneous information bits, and u_k and $\hat{u}_k$ denote the kth transmitted and decoded information bits, respectively.

To provide a consistent measure of the weak-light reception level under different received count rates, the received count rate was further converted into the equivalent number of detected photons per information bit. For the frame structure consisting of 16-PPM and 15 guard slots, the effective PPM pulse repetition rate is given by

$$f_p = \frac{f_{\text{slot}}}{M + G} \tag{8}$$

where f_{slot} is the slot rate, M is the PPM order, and G is the number of guard slots. In this work, f_{slot} = 400 M Hz, M = 16, G = 15, giving an effective PPM pulse repetition rate of approximately 12.90 MHz.

For a non-photon-number-resolving single-photon detector, when the received count rate is R_c, the click probability per pulse is

$$p_{\text{click}} = \frac{R_c}{f_p} \tag{9}$$

For a given mean number of detected photons, the number of photon arrivals within a single detection window can be described by a Poisson distribution [4,14]:

$$P(N = n) = \frac{\mu^n}{n!} \exp(-\mu^n), n = 0, 1, 2, \ldots, \tag{10}$$

where μ is the equivalent number of detected photons per pulse. For a non-photon-number-resolving detector, the no-detection event corresponds to N = 0. Therefore, the click probability per pulse is

$$p_{\text{click}} = 1 - \text{P}(0) \tag{11}$$

Under the assumption of Poisson photon-arrival statistics, the relationship between the click probability and the equivalent number of detected photons per pulse is

$$p_{\text{click}} = 1 - \exp(-\mu) \tag{12}$$

Thus,

$$\mu = -\ln(1 - p_{\text{click}}) \tag{13}$$

The equivalent number of detected photons per information bit can then be expressed as

$$n_b = \frac{\mu f_p}{R_b} \tag{14}$$

where R_b is the data rate.

2.3. Atmospheric Channel Characterization Method

To characterize the time-varying behavior of the free-space channel under closed-loop tracking, we used a time-to-digital converter (TDC) to record the arrival times of single-photon detection events. The pulse click probability was calculated over a fixed statistical time window and then used to estimate the equivalent number of detected photons per pulse $\mu(t)$. Taking the mean equivalent number of detected photons $\overline{\mu}$ over the observation period as the reference, the normalized time-varying channel gain is defined as

$$h(t) = \frac{\mu(t)}{\overline{\mu}} \tag{15}$$

where $h(t)$ describes the relative temporal variation in the received signal under closed-loop tracking.

The received-signal intensity fluctuations induced by atmospheric turbulence are characterized by the scintillation index, which is defined as [32]. Based on the equivalent number of detected photons, the scintillation index can be expressed as

$$\sigma_I^2 = \frac{\langle \mu^2(t) \rangle}{\langle \mu(t) \rangle^2} - 1 \tag{16}$$

where $\langle \cdot \rangle$ denotes time averaging. A larger scintillation index indicates more pronounced relative fluctuations in the received signal intensity.

In addition to the magnitude of intensity fluctuations, the duration of persistent fades is another important parameter for characterizing the temporal behavior of the channel. Taking the mean equivalent number of detected photons as the reference, the normalized received signal is expressed in logarithmic form as

$$F(t) = 10 \log_{10} h(t) = 10 \log_{10} \left[\frac{\mu(t)}{\overline{\mu}} \right] \tag{17}$$

In this work, -3, -6, and -10 d B are used as the fading thresholds. When $L(t)$ remains continuously below a given threshold L_{th}, the corresponding time interval is defined as a fading event. The duration of the ith fading event is expressed as

$$T_{\text{fade},k} = t_{\text{end},k} - t_{\text{start},k} \tag{18}$$

where $t_{i,\text{start}}$ and $t_{i,\text{end}}$ denote the start and end times of the fading event, respectively.

For a given fading threshold, the cumulative fading probability is defined as the ratio of the total duration of all fading events to the effective observation time, i.e.,

$$P_{\text{fade}}(F_{\text{th}}) = \frac{\sum_{k=1}^{N_f} T_{\text{fade},k}}{T_{\text{obs}}} \tag{19}$$

where N_{fade} denotes the number of fading events identified at the corresponding threshold, and T_{total} denotes the total observation time.

3. Results

3.1. Atmospheric Channel Characterization

We first established a 12 km free-space optical (FSO) link and achieved closed-loop tracking at both the transmitter and receiver terminals. During link establishment, the transmitter performed coarse pointing adjustment via a two-axis gimbal, steering the transmitted beam into the receiver's acquisition field of view (FOV). Once the receiver captured the beacon spot, a piezoelectric fine-pointing mechanism was activated for high-precision pointing correction. Subsequently, the transmitter and receiver sequentially switched to closed-loop tracking mode, maintaining stable link pointing through spot position feedback.

During closed-loop fine tracking, the tracking camera continuously measures the centroid displacement of the beacon spot. This displacement is used as the pointing-error signal and fed into the fine-tracking control loop, where the fast steering mirror (FSM) provides the corresponding angular correction. The maximum deflection range of the FSM determines the angular correction range of the fine-tracking system, while its dynamic response affects the ability to compensate for time-varying pointing disturbances. Under closed-loop operation, the pointing stability at the transmitter and receiver was

characterized by continuously recording the spot-centroid position and calculating the RMS tracking error.

Figure 3 shows the temporal variations in the beam centroid positions in the x- and y-directions at both terminals. The RMS tracking errors calculated from the centroid fluctuations were 1.67 and 2.00 μrad in the x- and y-directions at the transmitter, and 0.38 and 0.77 μrad at the receiver, corresponding to two-dimensional RMS tracking errors of 2.60 and 0.86 μrad, respectively. Previous studies have indicated that the RMS pointing error of a laser communication terminal is typically on the order of one-tenth of the beam divergence angle [33]. The RMS tracking errors at both terminals in this experiment were below this level, indicating stable closed-loop tracking performance.

To further evaluate the influence of the tracking process on received-intensity fluctuations, a power-budget analysis was performed for the tracking optical paths at both the transmitter and receiver, based on the link power model described in Section 2.1. The results are summarized in Table 3.

Table 3. Power Budget for the Bidirectional Tracking Links.

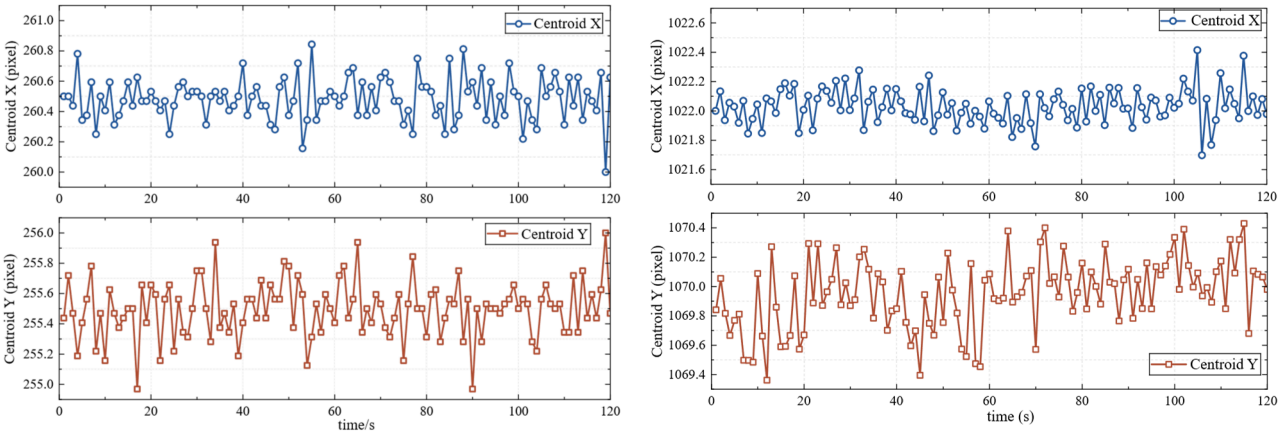
Parameter	450 nm	1550 nm
Transmit Power/dBm	−14.0	23
Received Power at the Tracking Camera/dBm	−53.0	−24.6
Minimum Detectable Power of the Tracking Camera [34]/dBm	−80.0	−75.0
Detection Margin/dB	27.0	50.4

Note: $\eta_t = \eta_r = 0.1$ are the overall optical efficiencies of the transmitter and receiver, respectively, and $\eta_{\mathrm{tr}} = 0.5$ is the tracking efficiency. Atmospheric attenuation is excluded from the received-power calculation.

As shown in Table 3, without accounting for atmospheric attenuation, the received powers of the 450 nm and 1550 nm tracking beams at the corresponding tracking cameras are −53.0 dBm and −24.6 dBm, respectively. These values correspond to detection margins of 27.0 dB and 50.4 dB relative to the minimum detectable powers of the cameras. Even when practical atmospheric attenuation is taken into account, both tracking optical paths still have relatively large power margins. Beam wander induced by atmospheric turbulence can affect tracking stability. The spot-centroid variations shown in Figure 4, together with the small RMS tracking errors under closed-loop operation, indicate that the fine-tracking system can effectively compensate for beam-position variations. The residual pointing errors after closed-loop correction are small, and their influence on received-power fluctuations is relatively limited. Therefore, under stable closed-loop tracking, the rapid photon-count variations subsequently recorded by the TDC are mainly used to characterize the received-intensity fluctuations induced by atmospheric turbulence.

After the closed-loop tracking system reached stable operation, we examined the atmospheric channel conditions during the experiment. The main meteorological parameters are summarized in Table 4. No precipitation, haze, or other adverse weather conditions were observed during the measurement period. The meteorological data were obtained from Ref. [35].

To characterize the received-intensity fluctuations over the atmospheric link, the transmitter continuously emitted optical pulses at a repetition rate of 10 MHz, and a time-to-digital converter (TDC) at the receiver recorded the single-photon detection events. Because turbulence-induced intensity fluctuations over long-haul atmospheric links typically exhibit millisecond-scale temporal variations [36], we accumulated the pulse-synchronized detection events within fixed-duration time windows to balance temporal resolution and photon-counting statistics. We then inferred the equivalent number of detected photons per pulse from the measured click probability.



(**a**) (**b**)

Figure 4. Temporal variations in the beam centroid positions in the x- and y-directions: (**a**) transmitter; (**b**) receiver.

Table 4. Meteorological conditions during the field experiment.

Parameter	Value
Experimental location	Shanghai, China
Experimental time	7 August 2026, 20:00–24:00
Temperature	30–31 °C
Horizontal visibility	≥10 km
Wind speed	9–10 m/s
Weather conditions	Good visibility with no apparent adverse weather

To examine the effect of the statistical time window on the characterization of received-intensity fluctuations, we processed three independent measurement records using time windows of 1, 10, and 50 ms, as shown in Figure 5. As the statistical window increased, the rapid fluctuations in the equivalent detected photon number were progressively smoothed, while local peaks and short-duration deep fades became less pronounced. Accordingly, the mean scintillation indices obtained with the 1, 10, and 50 ms windows were 0.271, 0.184, and 0.066, respectively. These results indicate that a larger statistical window produces a stronger time-averaging effect and therefore reduces the temporal resolution for capturing rapid channel fluctuations. At a pulse repetition rate of 10 MHz, a 1 ms statistical window contains approximately 1×10^4 pulse periods, providing a sufficiently large sample size for estimating the pulse detection probability and the equivalent number of detected photons. Meanwhile, the 1 ms timescale preserves adequate temporal resolution for millisecond-scale received-intensity fluctuations and avoids the pronounced temporal averaging introduced by longer statistical windows. Considering both the accuracy of the statistical estimation and the temporal resolution of channel fluctuations, a 1 ms statistical window was adopted for the subsequent analyses of the scintillation index and fading characteristics. Using this window, the scintillation indices of the three measurement records were 0.274, 0.263, and 0.275, respectively, with a mean value of 0.271. The similar scintillation indices indicate comparable levels of received-intensity fluctuations among the three records.

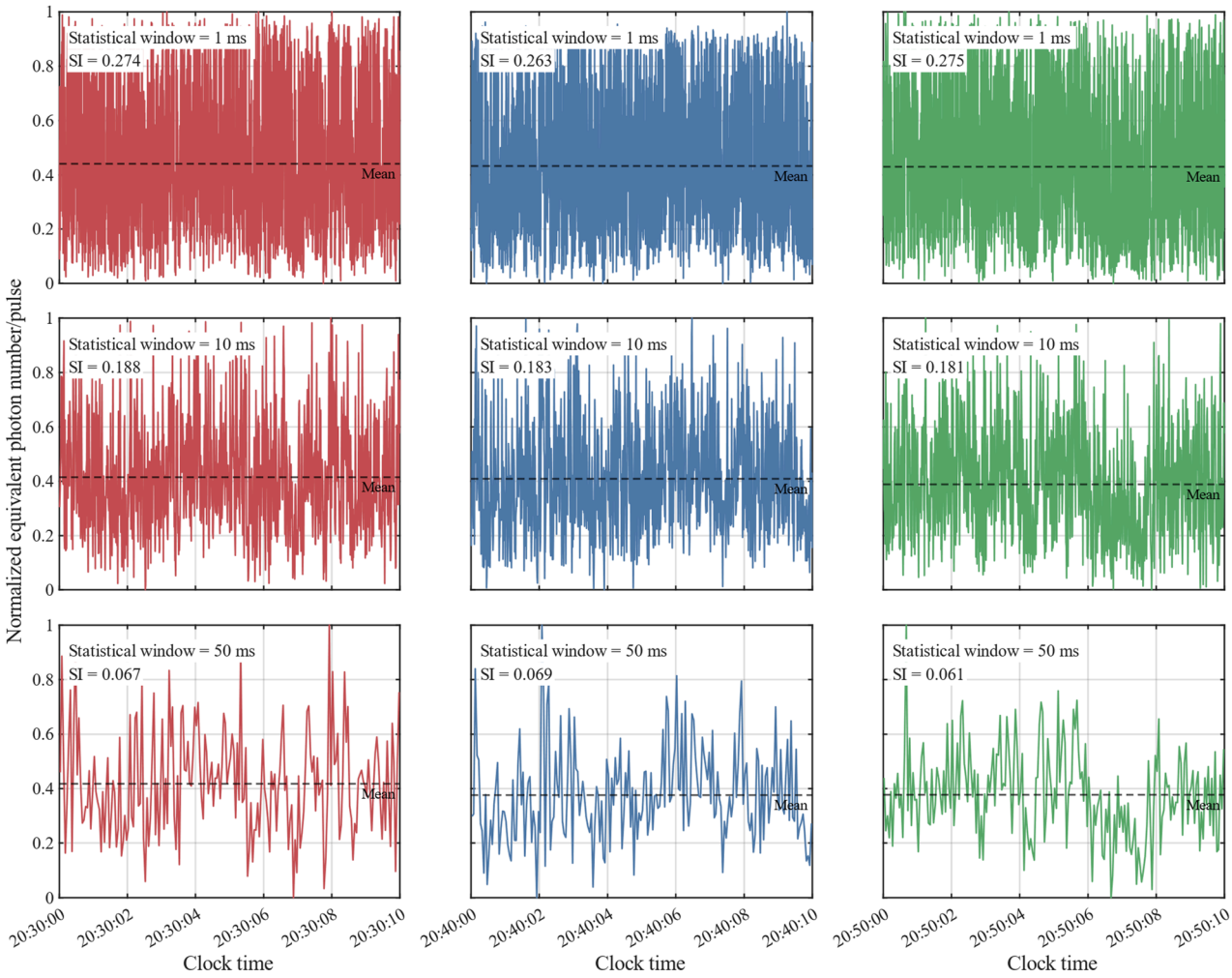


Figure 5. Temporal variations in the equivalent number of detected photons for three measurement records using statistical windows of 1, 10, and 50 ms. The columns represent the three measurement records, while the rows represent the three statistical windows. (The dashed lines indicate the mean values).

To further characterize the temporal behavior of received-intensity fading, we used thresholds of −3, −6, and −10 dB relative to the mean received intensity to identify fade events. A fade event was defined as a continuous interval during which the received intensity remained below the corresponding threshold. The resulting statistics are shown in Figure 6. The cumulative fade probabilities at the −3, −6, and −10 dB thresholds were 19.26%, 4.41%, and 0.52%, respectively. At the −3 dB threshold, the median and 90th-percentile fade durations were 3.0 and 10.0 ms, respectively, with a maximum duration of 40 ms. At the −6 dB threshold, the median and 90th-percentile fade durations were 2.0 and 6.0 ms, respectively, and the maximum duration was 20 ms. When the threshold was further reduced to −10 dB, the median and 90th-percentile fade durations decreased to 1.0 and 3.2 ms, respectively, with a maximum duration of 6 ms. These results indicate that both the fade probability and the number of fade events decrease markedly as the fading threshold becomes deeper. Meanwhile, the durations of deep-fade events also tend to become shorter. Nevertheless, continuous fades on the millisecond timescale remain present in the link.

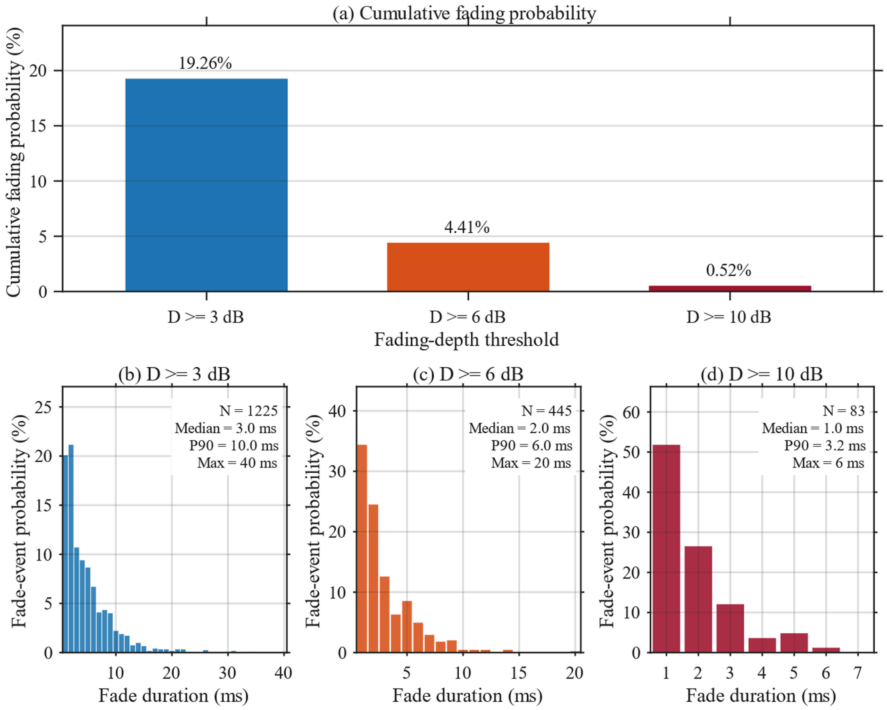


Figure 6. Time fractions and fade-duration distributions under different fading thresholds across three observation records. (**a**) Cumulative time fractions for fading thresholds of −3, −6, and −10 dB relative to the mean received intensity, defined as the fraction of effective observation time during which the received intensity remained below the corresponding threshold. (**b**–**d**) Conditional probability distributions of fade durations at the three thresholds. N denotes the number of detected fade events; Median, P90, and Max denote the median, 90th-percentile, and maximum fade durations, respectively.

The above results indicate that, even under stable closed-loop tracking, the 12 km horizontal atmospheric link exhibits pronounced received-intensity fluctuations and continuous fades on the millisecond timescale. Such temporally correlated fades may impair consecutive communication symbols over short time intervals, leading to burst errors and degraded SCPPM decoding performance. Accordingly, the following section compares the communication performance of the non-interleaved scheme with that of matrix and convolutional interleaving schemes.

3.2. Performance Analysis of Channel Interleaving

According to the atmospheric channel measurements presented in Section 3.1, fade events in the link occurred predominantly on the millisecond timescale. Taking the −3 dB threshold as an example, the median fade duration was 3.0 ms. Most fade events lasted less than 10 ms, whereas only a small number exhibited long-duration tails, with a maximum observed duration of 40 ms. For the 16-PPM format with 15 guard slots used in this work, a slot rate of 400 MHz corresponds to a PPM symbol duration of 77.5 ns. Therefore, continuous fades on the millisecond timescale can affect a large number of adjacent PPM symbols within a short interval and lead to burst errors.

To mitigate these temporally correlated fades, we employed several matrix and convolutional interleaving configurations with different interleaving scales. The matrix interleaving depths were set to 32, 64, and 128 to progressively distribute consecutive symbols across a larger number of SCPPM codewords. For convolutional interleaving, N was set to 15, 30, and 63, corresponding to maximum temporal spans of approximately 4.10, 8.50, and 18.16 ms, respectively. These temporal spans cover the dominant range of millisecond-scale fading observed in the link. This enables burst errors caused by continuous atmospheric

fading to be more effectively dispersed and facilitates further analysis of the relationship between interleaving scale and the measured fading characteristics.

To evaluate the effect of channel interleaving on the performance of the field photon-counting communication system, all interleaving schemes were tested over the same 12 km outdoor link under identical system configurations. The SCPPM coding, PPM, single-photon detection, TDC acquisition, receiver processing, and BER measurement parameters were kept unchanged, with only the channel interleaving configuration varied. All measurements were conducted within the same field-test period, during which the link remained under stable closed-loop tracking, and the overall meteorological conditions were similar. Because atmospheric turbulence is inherently random and time-varying, unavoidable differences existed in the instantaneous channel conditions at different measurement times. Therefore, the comparison presented in this work reflects the communication performance of different interleaving schemes under identical system parameters and broadly similar atmospheric conditions.

Each BER data point was measured using approximately 2×10^6 bits. To ensure a consistent comparison of the receiver performance among different interleaving schemes, the BER measured over the finite test sequence was used as the performance metric. The lowest received signal level at which no bit errors were observed was defined as the lowest zero-observed-BER operating point, and the corresponding equivalent number of detected photons per information bit was used to characterize the receiver sensitivity.

Figure 7 shows the BER as a function of the received photon count rate for the non-interleaved scheme, matrix interleaving with different depths, and convolutional interleaving with different configurations. Overall, the BER decreases with increasing received photon count rate for all schemes. However, the BER transition regions vary noticeably among the interleaver configurations. Compared with the non-interleaved scheme, the BER curves shift toward lower received photon count rates when channel interleaving is applied. This indicates that interleaving disperses burst errors caused by continuous atmospheric fading and reduces the concentration of errors within individual SCPPM codewords, thereby improving the BER performance of the system. In addition, increasing the matrix interleaving depth or the number of convolutional-interleaver branches generally reduces the received photon count rate required to reach the low-BER region. These results indicate that the interleaver configuration has a noticeable effect on system performance under atmospheric turbulence.

For matrix interleaving, the BER curves gradually shifted toward lower received photon count rates as the interleaving depth increased from 32 to 64 and 128. The received photon count rates required to reach the lowest zero-observed-BER operating point were 11.50, 10.80, and 10.58 Mcps for Matrix-32, Matrix-64, and Matrix-128, respectively. The corresponding equivalent detected photon numbers were 1.11, 0.91, and 0.86 detected photons per bit. These results show that a larger matrix interleaving depth distributes consecutively impaired symbols across a greater number of SCPPM codewords. This reduces the concentration of burst errors within each codeword and enables reliable decoding at lower received signal levels. Among the three matrix interleaving configurations, Matrix-128 achieved the lowest zero-observed-BER operating point. However, the additional improvement became smaller as the interleaving depth increased from 64 to 128, indicating diminishing gains from further increasing the matrix interleaving depth under the present experimental conditions.

For convolutional interleaving, the BER curves also gradually shifted toward lower received photon count rates as the number of branches N increased from 15 to 30 and 63. Conv-15 showed a pronounced BER decrease only at relatively high received photon count rates. When N increased to 30, the BER transition region shifted toward lower

count rates. A further increase to $N = 63$ resulted in additional BER improvement at low received photon count rates. The lowest zero-observed-BER operating points for Conv-15, Conv-30, and Conv-63 were 12.10, 11.60, and 11.50 Mcps, respectively, corresponding to 1.39, 1.15, and 1.11 detected photons per bit. As discussed in the preceding analysis of the convolutional-interleaving timescale, increasing N spreads adjacent symbols over a wider temporal range. As a result, burst errors caused by continuous turbulence-induced fading are redistributed across more data positions after deinterleaving, thereby enabling reliable decoding at lower received signal levels.

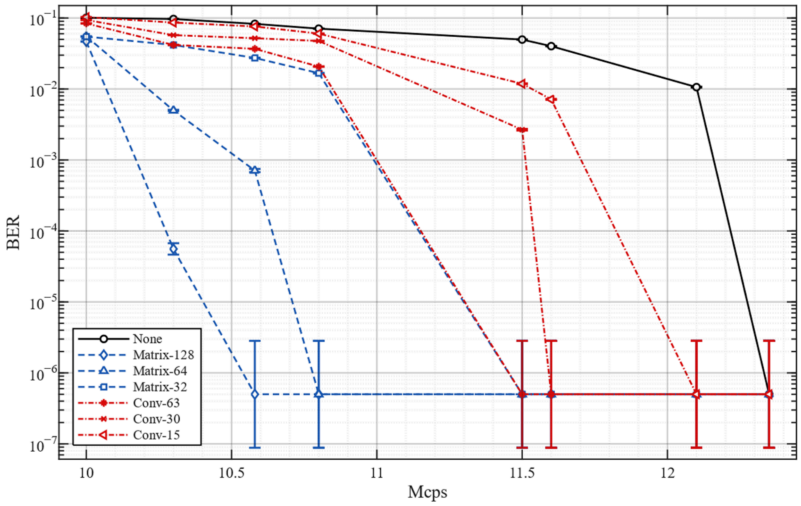


Figure 7. Bit error rate (BER) as a function of received count rate for different interleaving schemes. The black solid line represents the case without interleaving. The blue dashed lines represent matrix interleaving, with different symbols corresponding to Matrix-128, Matrix-64, and Matrix-32. The red dash-dotted lines represent convolutional interleaving, with different symbols corresponding to Conv-63, Conv-30, and Conv-15. Each data point was obtained from 2×10^6 bits, and the error bars indicate the 95% confidence intervals calculated using the Wilson score method.

Among the tested interleaving schemes, Matrix-128 achieved the lowest zero-observed-BER operating point under the present experimental conditions. To ensure a consistent comparison of receiver sensitivity among different interleaving schemes, the same test-sequence length was used for all schemes, and the lowest received signal level at which no bit errors were observed was adopted as the sensitivity criterion. Let n_0 and n_i denote the equivalent numbers of detected photons per information bit for the no-interleaving case and the ith interleaving scheme, respectively. The sensitivity gain is then defined as

$$G_i = 10 \log_{10} \left(\frac{n_0}{n_i} \right) \tag{20}$$

Table 5 summarizes the received photon count rate and detected photons per bit at the lowest zero-observed-BER operating point for each scheme, together with the corresponding receiver-sensitivity improvement relative to the non-interleaved scheme.

As shown in Table 5, without interleaving, the system required a received photon count rate of 12.35 Mcps to reach the lowest zero-observed-BER operating point, corresponding to 1.58 equivalent detected photons per bit. After channel interleaving was applied, the required received signal level decreased for all tested schemes. For convolutional interleaving, the equivalent detected photon numbers for Conv-15, Conv-30, and Conv-63 decreased to 1.39, 1.15, and 1.11 photons per bit, corresponding to sensitivity improvements of 0.55, 1.38, and 1.52 dB relative to the non-interleaved scheme, respectively. For matrix interleaving, the corresponding values for Matrix-32, Matrix-64, and

Matrix-128 were 1.11, 0.91, and 0.86 photons per bit, with sensitivity improvements of 1.52, 2.40, and 2.64 dB, respectively. Overall, increasing the matrix interleaving depth or the number of convolutional-interleaver branches reduced the received signal level required to reach the lowest zero-observed-BER operating point. Under the present experimental conditions, Matrix-128 achieved the lowest equivalent detected photon number and the largest sensitivity improvement among the tested schemes.

Table 5. Comparison of receiver sensitivity at the lowest zero-observed-BER operating point for different interleaving schemes.

Interleaving Scheme	Count Rate at the Lowest Zero-Observed-BER Operating Point (Mcps)	Detected Photons/Bit	Sensitivity Improvement/dB
No interleaving	12.35	1.58	0
Matrix-32	11.50	1.11	1.52
Matrix-64	10.80	0.91	2.40
Matrix-128	10.58	0.86	2.64
Conv-15	12.10	1.39	0.55
Conv-30	11.60	1.15	1.38
Conv-63	11.50	1.11	1.52

In addition, to more clearly illustrate the effect of channel interleaving on temporally correlated error behavior, we selected the non-interleaved scheme as the reference and Matrix-128, which achieved the best performance among the tested configurations, for time-domain comparison. Figure 8 shows the temporal variations in the received photon count rate and BER for the two schemes. The received photon count rates remained within a similar range in both measurements. Without interleaving, the BER was mainly on the order of 10^{-2}–10^{-1} and exhibited pronounced temporal fluctuations. With Matrix-128, most statistical intervals reached the zero-observed-BER condition, while only a few isolated BER peaks were observed. These results indicate that, at comparable received photon count rates, Matrix-128 disperses burst errors caused by continuous fading and substantially reduces the BER over most observation intervals.

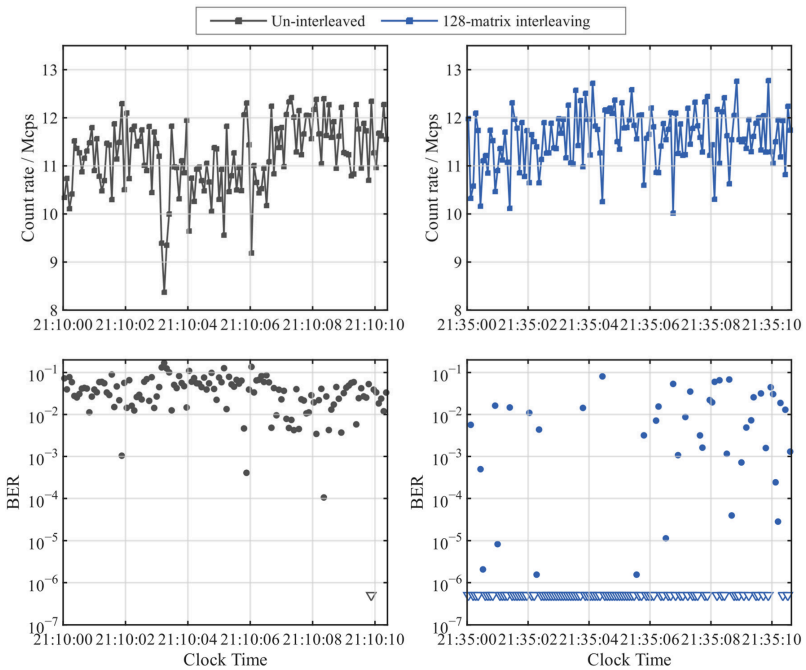


Figure 8. Temporal variation in BER for the non-interleaved and Matrix-128 interleaving schemes.

4. Discussion

Temporally correlated fading in practical atmospheric links is an important factor affecting the performance of photon-counting communication systems. The measured fades in this experiment mainly occurred on a millisecond timescale. For the −3 dB fading threshold, the median and 90th-percentile fade durations were 3.0 ms and 10.0 ms, respectively, indicating pronounced temporal persistence of deep fades. In comparison, the PPM symbol period of the communication system was only 77.5 ns. Therefore, a single millisecond-scale fading event can affect a large number of consecutive PPM symbols, causing errors to be concentrated within a limited number of SCPPM codewords. Channel interleaving redistributes coded symbols over time and thereby reduces the concentrated impact of a single fading event on an individual codeword. Experimental results show that the decoding performance at lower received photon levels improves as the interleaving scale increases. This result indicates that a larger temporal interleaving span can effectively mitigate the concentrated effect of persistent fades on individual codewords and improve the system resilience to temporal channel fading.

The performance improvement obtained with increasing interleaving scale does not increase linearly with interleaving depth. For matrix interleaving, increasing the interleaving depth from 32 to 64 reduces the equivalent detected photon level at the lowest zero-observed-BER operating point from 1.11 to 0.91 detected photons per bit. When the interleaving depth is further increased to 128, this value decreases only slightly to 0.86 detected photons per bit. A similar trend is observed for convolutional interleaving, for which Conv-30 and Conv-63 require 1.15 and 1.11 detected photons per bit, respectively. These results indicate that once the interleaving span becomes sufficiently large to cover most of the persistent fading events in the link, further extending the temporal dispersion of coded symbols provides progressively smaller additional performance gains.

Increasing the interleaving scale also increases the required memory and associated time overhead. For matrix interleaving, when the interleaving depth is increased from 64 to 128, the theoretical buffer requirement increases from 241,920 to 483,840 PPM symbols, whereas the sensitivity gain improves only from 2.40 to 2.64 dB. A similar trend is observed for convolutional interleaving. Increasing the configuration from Conv-30 to Conv-63 raises the theoretical buffer requirement from 54,810 to 117,180 PPM symbols, while providing only a marginal improvement in receiver sensitivity. Thus, as the interleaving scale continues to increase, the performance gain gradually saturates, whereas the required memory resources and associated time scale continue to grow. For real-time communication systems, the selection of interleaving parameters should therefore consider the channel fading time characteristics, receiver performance, and available hardware buffer resources. In this work, deinterleaving and SCPPM decoding were performed offline. Therefore, the reported buffer requirements and time scales are intended to characterize the theoretical implementation overhead of different interleaving configurations rather than the measured end-to-end processing latency of a real-time hardware system.

The field experiment was conducted over a 12 km urban horizontal free-space optical (FSO) link. Long-distance near-ground horizontal propagation can produce pronounced received-intensity fluctuations and temporally correlated deep fades, providing a realistic atmospheric environment for terrestrial validation of turbulence-mitigation techniques in photon-counting communication systems. However, horizontal links differ from practical satellite optical uplinks in both propagation geometry and the spatial distribution of atmospheric turbulence along the propagation path. Previous satellite–ground FSO studies have shown that atmospheric turbulence in space optical uplinks mainly affects the near-ground portion of the propagation path, while scintillation, beam wander, and received-intensity fluctuations are influenced by factors such as the zenith angle and the vertical

turbulence profile [37]. In contrast, the 12 km near-ground horizontal link used in this work propagates over a long distance within the lower atmosphere, resulting in propagation geometry and turbulence distributions that differ from those of practical space optical uplinks [15,38]. Therefore, the field experiment presented here is not intended as a direct equivalent of a satellite uplink channel. Instead, it uses the temporally correlated intensity fading and burst errors generated by a real atmospheric link to experimentally evaluate the performance of channel interleaving in high-speed photon-counting communication.

5. Conclusions

In this study, we conducted a high-speed PPM field communication experiment over a 12 km urban horizontal free-space link using a room-temperature single-photon detector. We experimentally evaluated the performance of different channel-interleaving schemes under real atmospheric turbulence conditions. The experimental results show that received-intensity fluctuations and persistent deep fades in the link lead to pronounced temporally correlated errors. Channel interleaving disperses burst errors across multiple SCPPM codewords, thereby reducing their concentration within individual codewords and improving system performance.

At a data rate of 25.8 Mbps, the receiver sensitivity without interleaving was 1.58 detected photons per bit. Both matrix and convolutional interleaving improved the communication performance to varying degrees. With a matrix interleaving depth of 128, the receiver sensitivity reached 0.86 detected photons per bit, corresponding to a sensitivity improvement of approximately 2.64 dB over the non-interleaved scheme. For convolutional interleaving with N = 63 branches, the receiver sensitivity reached 1.11 detected photons per bit, corresponding to a sensitivity improvement of approximately 1.52 dB. Under the channel conditions and parameter settings considered in this experiment, the Matrix-128 scheme provided the largest sensitivity improvement among all tested configurations.

The results show that, without changing the modulation and coding structures, an appropriate increase in the channel-interleaving scale can improve the tolerance of high-speed photon-counting communication systems to burst errors induced by atmospheric turbulence. The 12 km field experiment further demonstrates the potential of room-temperature single-photon detectors for long-haul, high-speed, photon-limited PPM communication. These results are also relevant to high-speed optical uplinks for applications such as on-orbit software updates, payload reconfiguration, file and command uploads, and future lunar and deep-space networking.

Author Contributions: Conceptualization, X.G. and J.H.; methodology, X.G., J.W. (Jincai Wu) and Y.L. (Yunpeng Liu); software, X.G. and H.B.; validation, X.G. and H.B.; formal analysis, X.G. and X.W.; investigation, X.G., Z.L., C.T. and Y.L. (Yuefeng Li); data curation, H.B. and X.Y.; writing—original draft preparation, X.G.; writing—review and editing, J.H.; visualization, X.G.; supervision, L.Z. and J.W. (Jianyu Wang); project administration, L.Z.; funding acquisition, L.Z. All authors have read and agreed to the published version of the manuscript.

Funding: Innovation Program for Quantum Science and Technology (2021ZD0300100); Shanghai Pilot Program for Basic Research—Chinese Academy of Science, Shanghai Branch; Cultivation Project of Shanghai Research Center for Quantum Sciences (LZPY2024); The Innovation Project of Shanghai Institute of Technical Physics, grant number CX-536.

Institutional Review Board Statement: Not applicable.

Informed Consent Statement: Not applicable.

Data Availability Statement: The original contributions presented in this study are included in the article. Further inquiries can be directed to the corresponding author.

Conflicts of Interest: The authors declare no conflicts of interest.

References

1. Kaushal, H.; Kaddoum, G. Optical Communication in Space: Challenges and Mitigation Techniques. *IEEE Commun. Surv. Tutor.* **2017**, *19*, 57–96. [CrossRef]
2. Mendenhall, J.A.; Candell, L.M.; Hopman, P.I.; Zogbi, G.; Boroson, D.M.; Caplan, D.O.; Digenis, C.J.; Hearn, D.R.; Shoup, R.C. Design of an Optical Photon Counting Array Receiver System for Deep-Space Communications. *Proc. IEEE* **2007**, *95*, 2059–2069. [CrossRef]
3. Huang, S.; Chitnis, D.; Chen, C.; Haas, H.; Khalighi, M.-A.; Henderson, R.K.; Safari, M. Single-Photon Counting Receivers for Optical Wireless Communications in Future 6G Networks. *IEEE Commun. Mag.* **2024**, *62*, 54–60. [CrossRef]
4. Moision, B.; Hamkins, J. *Coded Modulation for the Deep-Space Optical Channel: Serially Concatenated Pulse-Position Modulation*; Interplanetary Network Progress Report 42-161; Jet Propulsion Laboratory, California Institute of Technology: Pasadena, CA, USA, 2005; pp. 1–25.
5. Jarzyna, M.; Kunz, L.; Zwoliński, W.; Jachura, M.; Banaszek, K. Photon Information Efficiency Limits in Deep-Space Optical Communications. *Opt. Eng.* **2024**, *63*, 041209. [CrossRef]
6. Khatri, F.I.; Robinson, B.S.; Semprucci, M.D.; Boroson, D.M. Lunar Laser Communication Demonstration Operations Architecture. *Acta Astronaut.* **2015**, *111*, 77–83. [CrossRef]
7. Edwards, B.L.; Antsos, D.; Biswas, A.; Reinhart, R.; Robinson, B.; Boroson, D.; Khatri, F.; Lichten, S. Addressing the High-Rate Deep Space Communications Shortfall in NASA's Space Technology Mission Directorate's Envisioned Future. In Proceedings of the 29th Ka and Broadband Communications Conference, Seattle, WA, USA, 24–27 September 2024.
8. Murphy, K. NASA Laser Terminal Enhances Views During Artemis II Mission. Available online: https://www.nasa.gov/missions/artemis/artemis-2/nasa-laser-terminal-enhances-views-during-artemis-ii-mission/ (accessed on 23 August 2026).
9. Hao, H.; Zhao, Q.-Y.; Huang, Y.-H.; Deng, J.; Yang, F.; Ru, S.-Y.; Liu, Z.; Wan, C.; Liu, H.; Li, Z.-J.; et al. A Compact Multi-Pixel Superconducting Nanowire Single-Photon Detector Array Supporting Gigabit Space-to-Ground Communications. *Light Sci. Appl.* **2024**, *13*, 25. [CrossRef] [PubMed]
10. Wollman, E.E.; Allmaras, J.P.; Beyer, A.D.; Korzh, B.; Runyan, M.C.; Narváez, L.; Farr, W.H.; Marsili, F.; Briggs, R.M.; Miles, G.J.; et al. An SNSPD-Based Detector System for NASA's Deep Space Optical Communications Project. *Opt. Express* **2024**, *32*, 48185–48198. [CrossRef] [PubMed]
11. Stevens, M.L.; Boroson, D.M. A Simple Delay-Line 4-PPM Demodulator with near-Optimum Performance. *Opt. Express* **2012**, *20*, 5270–5280. [CrossRef] [PubMed]
12. Shtyrkova, K.; Burton, C.D.; Schulein, R.T.; Gaschits, I.; Romkey, B.; Caplan, D.O.; Murphy, D.V.; Robinson, B.S. Design and Performance of a 40W Uplink Laser Transmitter for NASA's O2O Laser Communications Mission. In Proceedings of the Free-Space Laser Communications XXXVII, San Francisco, CA, USA, 25–30 January 2025; Volume 13355. [CrossRef]
13. Wen, G.; Huang, J.; Zhang, L.; Li, C.; Wen, T.; Wang, J. A High-Speed and High-Sensitivity Photon-Counting Communication System Based on Multichannel SPAD Detection. *IEEE Photonics J.* **2021**, *13*, 7900310. [CrossRef]
14. Huang, J.; Li, C.; Dai, J.; Shu, R.; Zhang, L.; Wang, J. Real-Time and High-Speed Underwater Photon-Counting Communication Based on SPAD and PPM Symbol Synchronization. *IEEE Photonics J.* **2021**, *13*, 7300209. [CrossRef]
15. Phuchortham, S.; Sabit, H. A Review of the Structure of Free-Space Optical Channel Models: Physical Meaning, Assumptions, and Atmospheric Conditions. *Photonics* **2026**, *13*, 425. [CrossRef]
16. Alimi, I.A.; Monteiro, P.P. Revolutionizing Free-Space Optics: A Survey of Enabling Technologies, Challenges, Trends, and Prospects of Beyond 5G Free-Space Optical (FSO) Communication Systems. *Sensors* **2024**, *24*, 8036. [CrossRef] [PubMed]
17. Sun, S.W.; Noh, J.H. End-to-End Performance Analysis of CCSDS O3K Optical Communication System Under Atmospheric Turbulence and Pointing Errors. *Aerospace* **2025**, *12*, 869. [CrossRef]
18. Xu, F.; Khalighi, A.; Caussé, P.; Bourennane, S. Channel Coding and Time-Diversity for Optical Wireless Links. *Opt. Express* **2009**, *17*, 872–887. [CrossRef] [PubMed]
19. Greco, J.A. Design of the High-Speed Framing, FEC, and Interleaving Hardware Used in a 5.4 km Free-Space Optical Communication Experiment. In Proceedings of the Free-Space Laser Communications IX, San Diego, CA, USA, 2–3 August 2009; Volume 7464. [CrossRef]
20. Fujita, S.; Okamoto, E.; Takenaka, H.; Endo, H.; Fujiwara, M.; Kitamura, M.; Shimizu, R.; Sasaki, M.; Toyoshima, M. Polar-Coded Transmission over 7.8-Km Terrestrial Free-Space Optical Links. *Photonics* **2023**, *10*, 462. [CrossRef]
21. Chang, Y.; Cai, S.; Wang, L.; Zhang, H.; Zhang, Z. Experimental Analysis of Reducing Outage Probability Using Deep Interleaving for Long-Distance FSO Systems. In Proceedings of the 2024 IEEE Opto-Electronics and Communications Conference (OECC), Melbourne, Australia, 30 June–4 July 2024; pp. 1–3. [CrossRef]

22. Boddeda, R.; Ghazisaeidi, A.; Bigo, S.; Rabeh, S.; Dovillaire, G.; Almonacil, S.; Mardoyan, H.; Renaudier, J. Tailoring Rate and Latency of Free Space Optical Systems to Turbulence Conditions with Probabilistic Constellation Shaping and Data Interleaving. In Proceedings of the Optical Fiber Communication Conference (OFC) 2024, San Diego, CA, USA, 24–28 March 2024; Paper Th3C.5. [CrossRef]
23. Gümüş, K.; van Vliet, V.; van den Hout, M.; Bradley, T.; Tangdiongga, E.; Okonkwo, C. Reducing Turbulence-Induced Outages in a Deployed Terrestrial Free-Space Optical Communication Link via Interleaving. *arXiv* **2026**, arXiv:2606.16855. [CrossRef]
24. Burton, A.; Ghassemlooy, Z.; Le Minh, H.; Arapoglou, P.-D. Physical Layer Simulator of the Deep Space to Ground High Photon Efficiency Optical Wireless Communications Link. In Proceedings of the First West Asian Colloquium on Optical Wireless Communications, Isfahan, Iran, 25 April 2018.
25. Downey, J.N.; Chahine, Y.K.; Tedder, S.A.; Katz, E.J.; Marsden, M.A.; Clapham, J.S. Performance of a Real-Time Photon Counting Optical Receiver in the Presence of Emulated Channel Fading. In Proceedings of the Free-Space Laser Communications XXXVI, San Francisco, CA, USA, 27 January–1 February 2024; Volume 12877. [CrossRef]
26. Wang, Z.; Zhang, Y.; Gu, H.; Han, C.; Yin, L.; Liang, Y. Time-Resolved Calibration of Photon Detection Efficiency and Afterpulse Probability in 100 MHz Gated InGaAs/InP Single-Photon Avalanche Diodes. *Photonics* **2025**, *12*, 534. [CrossRef]
27. Ceccarelli, F.; Acconcia, G.; Gulinatti, A.; Ghioni, M.; Rech, I.; Osellame, R. Recent Advances and Future Perspectives of Single-Photon Avalanche Diodes for Quantum Photonics Applications. *Adv. Quantum Technol.* **2021**, *4*, 2000102. [CrossRef]
28. Dhruv; Kaushal, H. A Review of Pointing Modules and Gimbal Systems for Free-Space Optical Communication in Non-Terrestrial Platforms. *Photonics* **2025**, *12*, 1001. [CrossRef]
29. Paudel, R.; Ghassemlooy, Z.; Le-Minh, H.; Rajbhandari, S. Modelling of Free Space Optical Link for Ground-to-Train Communications Using a Gaussian Source. *IET Optoelectron.* **2013**, *7*, 1–8. [CrossRef]
30. Das, B.; Sarma, M.P.; Sarma, K.K. Different Aspects of Interleaving Techniques in Wireless Communication. In *Intelligent Applications for Heterogeneous System Modeling and Design*; Sarma, K.K., Sarma, M.P., Sarma, M., Eds.; IGI Global: Hershey, PA, USA, 2015; pp. 335–374. [CrossRef]
31. Moision, B.; Biswas, A. *Memory Requirements to Mitigate Fading Losses on an Optical Channel*; Jet Propulsion Laboratory, California Institute of Technology: Pasadena, CA, USA, 2007.
32. Borah, D.K.; Boucouvalas, A.C.; Davis, C.C.; Hranilovic, S.; Yiannopoulos, K. A Review of Communication-Oriented Optical Wireless Systems. *EURASIP J. Wirel. Commun. Netw.* **2012**, *2012*, 91. [CrossRef]
33. Yu, H.; Lu, S.; Hu, Q.; Fan, Y.; Zhu, F.; Xia, H.; Li, J.; Sun, J.; Hou, X.; Chen, W.; et al. In-Orbit Intersatellite Laser Communication Experiment Based on Compound-Axis Tracking. *Chin. Opt. Lett.* **2025**, *23*, 040605. [CrossRef]
34. Bai, S.; Qiang, J.; Zhang, L.; Wang, J. Optimization of Spatial Acquisition Systems for Low-Light-Level Robustness in Space Optical Communications. *Opt. Lett.* **2015**, *40*, 3750. [CrossRef] [PubMed]
35. Menne, M.J.; Noone, S.; Casey, N.W.; Dunn, R.H.; McNeill, S.; Kantor, D.; Thorne, P.W.; Orcutt, K.; Cunningham, S.; Risavi, N. *Global Historical Climatology Network-Hourly (GHCNh), Version 1*; Shanghai Pudong Station (CHI0000ZSPD), 7 August 2026 Subset; NOAA National Centers for Environmental Information: Asheville, NC, USA, 2023. [CrossRef]
36. Kang, H.J.; Yang, J.; Chun, B.J.; Jang, H.; Kim, B.S.; Kim, Y.-J.; Kim, S.-W. Free-Space Transfer of Comb-Rooted Optical Frequencies over an 18 Km Open-Air Link. *Nat. Commun.* **2019**, *10*, 4438. [CrossRef] [PubMed]
37. Maharjan, N.; Devkota, N.; Kim, B.W. Atmospheric Effects on Satellite–Ground Free Space Uplink and Downlink Optical Transmissions. *Appl. Sci.* **2022**, *12*, 10944. [CrossRef]
38. Czerwinski, A. Atmospheric Modeling of Free-Space Optical Transmission: Satellite Downlinks and Horizontal Channels. *Opt. Quantum Electron.* **2025**, *57*, 577. [CrossRef]

Disclaimer/Publisher's Note: The statements, opinions and data contained in all publications are solely those of the individual author(s) and contributor(s) and not of MDPI and/or the editor(s). MDPI and/or the editor(s) disclaim responsibility for any injury to people or property resulting from any ideas, methods, instructions or products referred to in the content.